

# Detection and Matching of Fiducial Markers under Highly Challenging Conditions

## Supplementary material

Lilian Calvet<sup>1</sup>, Pierre Gurdjos<sup>2</sup>, Carsten Griwodz<sup>1</sup>, and Simone Gasparini<sup>2</sup>

<sup>1</sup>Simula Research Laboratory, Oslo, Norway {lcalvet, griff}@simula.no

<sup>2</sup>University of Toulouse, France {pgurdjos, sgaspari}@enseeiht.fr

### 1. Introduction

In this work we presented a new fiducial system based on concentric circles. We showed that the proposed system provides a higher detection accuracy as well as a good recognition rate in many highly challenging conditions, ranging from severe occlusions to motion blur to illumination changes.

Table 1 summarizes and compares the main features of the principal systems that can be found in the literature with the proposed one. Our method, like most of the others, does not need the camera to be calibrated for detecting the markers. Only RuneTag needs the camera to be calibrated (known focal length) in order to detect the markers. On the other hand, another interesting feature that a fiducial system can supply is the number of reference points that it can provide in order to, *e.g.*, calibrate the camera.

The encoding capacity refers to the total number of unique fiducial markers. We remind that the proposed fiducial markers consist of circular barcodes. In the current implementation, a ring (black or white) holds a 1-bit information, its width being 0.10 or 0.15 (w.r.t. the outer circle of unit radius). In such a way, a library of fiducial markers composed of  $N$  rings has  $2^{2N-1}$  unique markers. Once a fiducial marker has been detected and its 1D signals along the cross sections have been rectified, the later are read in a robust manner via the distance proposed in [3] then delivering the marker ID associated to a marker profile (examples of these profiles are illustrated in Figure 1).

The robustness to occlusion and motion blur is a key feature for any fiducial system as it allows the camera to operate in challenging conditions and under unconstrained motions. The proposed method has been proved to be robust to occlusions up to 60% of the marker, whereas only PRASAD and RuneTag have shown some (limited) ability to deal with large occlusions. Moreover, thanks to the circular pattern, the proposed marker happens to be robust to severe linear motion blurs due to rapid translations of the camera.

Last but not least, our system will be soon released as an open source project with both a CPU and a GPU implementation. To this day, only ARTKPlus provides an open source SDK for marker detection and camera pose estimation. Today, our CPU implementation is able to deliver a frame rate of 4 fps on one CPU (i5-4590, 3Ghz) core on a  $1280 \times 720$  image, which has been raised to 11 fps using the so far incomplete GPU (NVidia GTX 980 Ti, CUDA 7.0) implementation.

The circular fiducial detection (cf. §3.1 of the submitted paper) is performed on a pyramid of images, which provides a trade-off between the search for distances between the edge of a ring and the ability to detect markers of various sizes and at a wide range of distances from the camera. In our experiments, we used pyramids of  $N = 4$  levels, where the image resolution is halved both in X and Y direction between levels. Once candidate markers are selected over all the pyramid levels, the circular fiducial validation (described in §3.2 of the submitted paper) including its identification are performed on the original image to ensure a maximum accuracy.

The GPU version replaces the implementation of the pyramid building phase completely, where the possible parallelization still allows a speedup from 720p to 1080p videos that is superlinear. In the detection stage, voting is handled on the GPU, but the incremental formation of convex arc segments remains on the CPU. Although only a few marker candidates remain after the detection stage, there lies a decent parallelization potential in the validation stage, which is due to a search step in the localization of the imaged center. Unfortunately, the GPU implementation is still incomplete. The system is currently

under further development in the context of an industrial innovation project for a real-time augmented reality application. The code is written in C++ (and CUDA’s C++ dialect for the GPU implementation) relying other open source libraries in order to provide an highly customizable solution and foster new camera tracking applications.

	Proposed	PRASAD[6]	RuneTag [1]	ARTKPlus [5]	Mono-spect. [7]
Free of camera calibration	✓	✓		✓	✓
Allows camera calibration	✓			✓	
# reference points per fiducial [min-max]	[1-3]	0	[5-129]	4	0
Encoding capacity	32 (3 rings) 128 (4 rings)	4	762 (Rune-43) 19152 (Rune-129)	512	825
Robust to occlusion	✓	✓	✓		
Robust to motion blur	✓	✓			✓
Open source release CPU	✓			✓	
Open source release GPU	✓				

Table 1. Summary of capabilities of existing fiducial systems. See text for details.

resolution	stages of detection	CPU	GPU
720p	loading, pyramid building	48.6 ms	8.5 ms
720p	candidate detection	152 ms	27.3 ms
720p	candidate validation/identification	58 ms	incomplete
1080p	loading, pyramid building	105 ms	12.8 ms
1080p	candidate detection	209 ms	45.9 ms
1080p	candidate validation/identification	61 ms	incomplete

Table 2. Comparison of CPU and GPU performance by stage, on a video showing up to 5 markers

To summarize, the capabilities of the proposed system are listed below.

- *Free of camera calibration*: the system does not require the intrinsic parameters of the camera to be known.
- *Allows camera calibration*: the geometry of an imaged fiducial provides constraints for the camera’s intrinsics estimation and, under “normal” shooting conditions, it can further provide the image of the circular points to constrain the camera calibration process (*e.g.*, the well-known plane-based calibration method).
- *Robust to occlusion*: the fiducial can be detected even if it is occluded in the views (*e.g.*, up to 60%).
- *Robust to motion blur*: in presence of a linear motion blur (*i.e.*, motion blur due to a fast camera translation), the proposed fiducial is orthogonal to the blur direction and can be still detected and identified.
- *Open source release*: the code will be soon released as open source with both a CPU and a fast GPU implementation.

This supplementary material is organized as follows: in Section 2 we provide further experimental evidences that proves the effectiveness of our method w.r.t. the other state-of-the-art methods. The rest of the Sections provides mathematical proofs to the different propositions stated in the submitted paper.

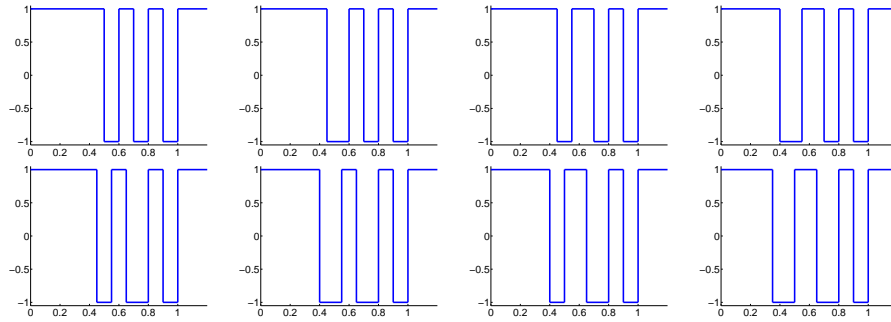


Figure 1. Functions of “profile” associated to the first eight profile models of our fiducial markers composed, in this case, of three rings (subset of the ones used in our experiments).

## 2. Further experiments

**Comparison with ARTKPlus.** The video provided as supplementary material shows the effectiveness of the proposed method. In the video the detection of the concentric marker is compared w.r.t. the ARTKPlus [8]. We chose ARTKPlus because among all the available open source solutions it is the one achieving better performances in terms of detection rate and computational time. In this experiment we used 4 markers for each solution placed on a plane at known positions, so that the relevant plane-induced homography can be estimated. For the ARTKPlus we first detected and identified all the markers and then we estimated the homography using all the detected marker corners following a DLT approach [4] (note that the homography can be then estimated even if only one marker is detected). For the proposed system, we detected the image of the four centers of the concentric circles and we used them to compute the homography. The image placed in between the markers can be then rectified in order to visually assess the quality of the estimated homography. Thanks to the accurate estimation of the image of the four centers of the concentric circles provided by our detection method, the homography can be robustly estimated and the rectified image is not affected by any significant jittering, whereas the rectified image computed with the ARTKPlus homography is more unstable. Moreover the video shows that the proposed method allows to detect the marker even in very challenging conditions, such as severe motion blur and sudden illumination changes.

**Other results on real images.** Some other results of the proposed system on real images are illustrated in Figure 2 (see the caption for details).

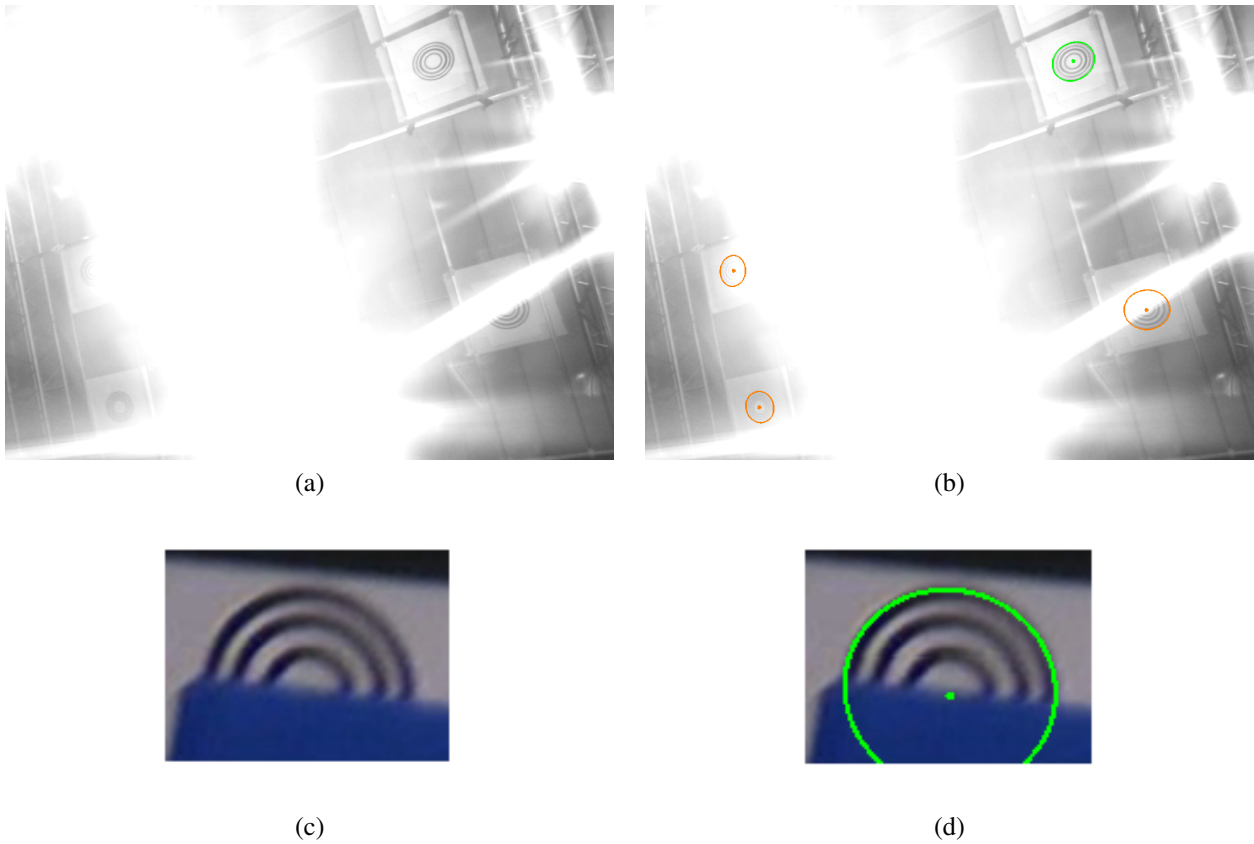


Figure 2. (a) View of a scene under very challenging lighting conditions. (b) Result of the detection algorithm. In this case, the hysteresis thresholds used by the Canny edge detection [2] are not the default values used in all the experiments conducted in this work and have been set to very low values. We want to emphasize here the fact that, even with very small values enabling to detect edge points with a very low contrast, thus leading to a large noise on their gradient direction, the construction of the field lines approximations is still reliable enough to detect the markers. However, as highlighted in the image, only one of them, drawn in green, has a reliable ID whereas the three other ones, drawn in orange, do not have a reliable identification: in the current implementation, a candidate that has not an univocal identification is rejected and considered as not detected. (c) An example of a challenging case where the marker is occluded and affected by motion blur. (d) Nevertheless, the marker is correctly detected and identified.

### 3. Proof of Proposition 1

As defined in the text, a field line of the gradient map  $\nabla_I$  defined on a domain  $D \subset \mathbb{R}^2$  through a point  $\mathbf{u}_0 \in D$  is a parametric curve  $\phi : U \subset \mathbb{R} \mapsto D$ , solution of the differential system

$$\begin{cases} \phi'(t) = \nabla_I(\phi(t)) \\ \phi(t_0) = \mathbf{u}_0 \end{cases} \quad (1)$$

where  $(t_0, \mathbf{u}_0) \in U \times \mathbb{R}^2$  defines an initial condition.

Remind that  $\Omega_r = B_1[\mathbf{0}] \setminus B_r(\mathbf{0})$  defines the surface of the ring between the two circles. Only for the proof, we consider that the ring is painted with a continuous gradation of gray hues (black is hue 0 and white is hue 1) as defined by the function  $\alpha : [-1, 1]^2 \rightarrow [0, 1]$  so we have  $\alpha(\mathbf{x}) = 1 - \|\mathbf{x}\|^2$  for all  $\mathbf{x} \in \Omega_r$  (interior of the ring),  $\alpha(\mathbf{x}) = 1$  for all  $\mathbf{x} \in B_r(\mathbf{0})$  (interior of the inner circle), and  $\alpha(\mathbf{x}) = 0$  for all  $\mathbf{x} \notin B_1[\mathbf{0}]$ . In the (continuous) image, the gray intensity is given by  $I(\mathbf{u}) = \alpha(H^{-1}(\mathbf{u}))$ .

**Item 1.** *In the continuous image, through any point in  $H(\Omega)$ , except the image of the circle centre, passes one and only one field line of  $\nabla_I$ .*

*Proof.* A field line is an integral curve, solution of the differential equation (1). Under the hypothesis of the Cauchy-Lipschitz theorem, through a point, it passes one and only one integral curve.  $\square$

**Item 2.** *Any field line of  $\nabla_I$  necessarily converges to one point on the inner ellipse.*

*Proof.* The field line through  $\mathbf{u} \in H(\Omega)$  can be seen as a sequence of infinitesimal displacements:

$$\begin{cases} \mathbf{u}_{i+1} = \lim_{d_i \rightarrow 0^+} \left( \mathbf{u}_i + d_i \frac{\nabla_I(\mathbf{u}_i)}{\|\nabla_I(\mathbf{u}_i)\|} \right) \\ \mathbf{u}_0 = \mathbf{u} \end{cases} \quad (2)$$

Assume  $r = 0$  so the inner circle is restricted to the circle's centre  $\mathbf{x}_C$  of the (two) circles composing the ring. Hence, the centre  $\mathbf{x}_C$  is the only point with hue  $\alpha = 1$ . Now, let  $\mathbf{u}_i \in H(\Omega_0)$  and let  $W(\mathbf{u}_i) \subset H(\Omega_0)$  denote its neighborhood. For any  $\mathbf{u}_i^j \in W(\mathbf{u}_i)$ , the gray intensity of  $I$  decreases the most significantly in the direction of the gradient  $\nabla_I(\mathbf{u}_i^j)$ . We can claim that the image  $\mathbf{u}_Q$  of the centre  $\mathbf{x}_C$  is the point where the sequence (2) converges since (i)  $\mathbf{u}_Q$  is the point where  $I(\mathbf{u}_Q)$  is maximum; (ii)  $\mathbf{u}_Q$  est is the unique singular point of  $I(H(\Omega))$ , i.e. the unique point such that  $\nabla_I(\mathbf{u}_Q) = 0$ , which entails that  $\nabla_I(\mathbf{u}_{i+1}) > \nabla_I(\mathbf{u}_i)$ ,  $\forall \mathbf{u}_i \neq \mathbf{u}_Q$ . In other words, *if  $\ell$  is a field line of  $\nabla_I$  then  $\ell$  converge to the image  $\mathbf{u}_Q$  of the ring's centre.*

When  $0 < r < 1$ , the (part of the) field lines on  $H(\Omega_r)$  are identical to those on  $H(\Omega_0)$  so, since the inner ellipse  $\mathcal{E}$  is an equipotential of  $I(H(\Omega_0))$ , i.e.,  $I(\mathbf{u}) = \text{const}$  for all  $\mathbf{u} \in \mathcal{E}$ , any field line of  $\nabla_I(H(\Omega_r))$  necessarily converges to one point on the inner ellipse, which ends the proof.  $\square$

### 4. Proof of equation (4)

A vector field  $F$  is said to be conservative if there exists a scalar field  $f$  such that  $F = \nabla f$ . By definition, the gradient field  $\nabla_I$  defined on  $H(\Omega)$  i.e., inside the imaged ring, is conservative. A key property is that the circulation of the flux along every closed loop in  $H(\Omega)$  is zero. Let  $\mathcal{T}_1$  and  $\mathcal{T}_2$  be two field lines of  $\nabla_I$ . Let  $\mathcal{A}_1$  and  $\mathcal{A}_2$  be the arcs of the outer and inner ellipses respectively. Let  $\partial\mathbf{S}$  be the closed boundary of the surface  $\mathbf{S}$  delimited by  $\mathcal{A}_1, \mathcal{T}_1, \mathcal{A}_2$  and  $\mathcal{T}_2$ , as shown in figure 5 of the submitted paper. By the conservative property, we have

$$0 = \oint_{\partial\mathbf{S}} \nabla_I \cdot d\boldsymbol{\sigma} = \int_{\mathcal{A}_1} \nabla_I \cdot d\boldsymbol{\sigma} + \int_{\mathcal{A}_2} \nabla_I \cdot d\boldsymbol{\sigma} + \int_{\mathcal{T}_1} \nabla_I \cdot d\boldsymbol{\sigma} + \int_{\mathcal{T}_2} \nabla_I \cdot d\boldsymbol{\sigma}$$

where  $d\boldsymbol{\sigma} = \mathbf{n}ds$  and  $\mathbf{n}$  is the unit normal to  $\mathbf{S}$  oriented towards the exterior of  $\mathbf{S}$ . At any point of the field lines  $\mathcal{T}_1$  and  $\mathcal{T}_2$ , the scalar product  $\nabla_I \cdot \mathbf{n}$  is zero since  $\nabla_I$  is tangent to the field lines. We hence have

$$\int_{\mathcal{A}_1} \nabla_I \cdot d\boldsymbol{\sigma} = - \int_{\mathcal{A}_2} \nabla_I \cdot d\boldsymbol{\sigma}$$

Since, at any point of the field lines  $\mathcal{A}_1$  and  $\mathcal{A}_2$ , the scalar product satisfies  $\nabla_I \cdot \mathbf{n} = \|\nabla_I\|$  since  $\nabla_I$  is parallel to the (unit) normal, using a arclength-parameterization of  $\mathcal{A}_1$  and  $\mathcal{A}_2$ , we obtain equation (4)

$$\int_{\mathcal{A}_1} \|\nabla_I\| ds = \int_{\mathcal{A}_2} \|\nabla_I\| ds$$

## 5. Proof of Proposition 2

A *canonical rectifying homography* for  $\mathbb{Q}$  is any homography  $\mathbb{G}$  of the image onto itself such that  $\mathbb{G}$  maps  $\mathbb{Q}$  to a unit circle centred at the origin, and the image  $\mathbf{u}_Q$  of the circle's centre to the origin. Equivalently said,  $\mathbb{G}$  maps the images of two concentric circles, one of which being  $\mathbb{Q}$ , to two concentric circles centred at the origin, the pre-image of  $\mathbb{Q}$  having radius 1 (the pre-image of  $\mathbf{u}_Q$  can be seen as a circle with zero radius). As a consequence, the original Euclidean geometry of the plane  $\Pi$  supporting the circle is recovered, up to a 2D translation, homothety and scaling. The proof is set up under the following hypotheses.

- H1: We assume the quasi-affine invariance of the circle(s), whose sufficient condition is that all of its (their) points lie in front of the camera.
- H2: We assume a camera with square pixels i.e., that the distance inter-pixels is the Euclidean distance.

Implicitly assuming a non-degenerate  $\mathbb{Q}$ , neither  $r$  or  $s$  in equations (6) and (7) of Proposition 2 can be zero. Indeed,

- $Q_{11} \neq 0$  and  $Q_{22} \neq 0$  since all eigenvalues of  $\mathbb{Q}$  are non-zero,
- Under hypothesis H1, regarding  $r$ , let

$$k_1 = Q_{11}u_Q^2 + Q_{22}v_C^2 - 1 = (\mathbf{u}_Q^\top, 1)\mathbb{Q}(\mathbf{u}_Q^\top, 1)^\top \quad (3)$$

Then  $k_1 \neq 0$ , since  $\mathbf{u}_Q$  is the image of the circle centre which is a point that do not lie on  $\mathbb{Q}$ .

- Under hypothesis H1-H2, regarding  $s$ , let

$$k_2 = Q_{11}u_Q^2 - 1 = (u_Q, 0, 1)\mathbb{Q}(u_Q, 0, 1)^\top \quad (4)$$

Then  $k_2 \neq 0$ , since  $(u_Q, 0)^\top$  is the orthogonal projection of  $\mathbf{u}_Q$  onto the semi-major axis of  $\mathbb{Q}$  which is a point that do not lie on  $\mathbb{Q}$ .

*Proof.* More generally, an homography  $\mathbb{A}$  is a *rectifying homography* if and only if it transforms the images  $\mathbf{J}_\pm$  of the circular (complex conjugate) point-pair of  $\Pi$  into the standard form  $\mathbb{A}\mathbf{J}_\pm \sim (1, \pm i, 0)^\top$ , where  $\sim$  refers to the projective equality and  $i = \sqrt{-1}$ , which is an invariant form in all Euclidean representations of  $\Pi$ . An equivalent necessary and sufficient condition is that the matrix  $\Sigma^* = (\mathbf{J}_+ \mathbf{J}_-^\top + \mathbf{J}_- \mathbf{J}_+^\top)$ , representing the image of the conic dual to the images of the circular point-pair [4, p.53], is transformed by  $\mathbb{A}$  into the standard form,

$$\mathbb{A}\Sigma^*\mathbb{A}^\top \sim \begin{bmatrix} 1 & 0 & 0 \\ 0 & 1 & 0 \\ 0 & 0 & 0 \end{bmatrix} \quad (5)$$

which is also the same in every Euclidean representation. The difference between the two rectifying homographies  $\mathbb{G}$  and  $\mathbb{A}$  is that  $\mathbb{G}$  is canonical while  $\mathbb{A}$  is not i.e., by applying  $\mathbb{A}$  to the two image ellipses corresponding the projections of two concentric circles, we obtain two concentric circles that are generally neither centered at the origin nor of unit radius.

It is well-known [4, p.42] that, as any rectifying homography, a canonical rectifying homography  $\mathbb{G}$  can be decomposed into a chain product of three homographies

$$\mathbb{G} = \mathbb{G}_\mathcal{E} \mathbb{G}_\mathcal{A} \mathbb{G}_\mathcal{P} \quad (6)$$

where the matrix

$$\mathbb{G}_\mathcal{P} = \begin{bmatrix} 1 & 0 & 0 \\ 0 & 1 & 0 \\ & & \mathbf{v}^\top \end{bmatrix} \quad (7)$$

is the projective component of  $G$  that maps  $\mathbf{v}$ , the vector of the vanishing line of  $\Pi$ , to its canonical form  $(0, 0, 1)^\top$  i.e., to infinity ; the matrix

$$\mathbf{G}_A = \begin{bmatrix} 1/b & -a/b & 0 \\ 0 & 1 & 0 \\ 0 & 0 & 1 \end{bmatrix} \quad (8)$$

is the affine component of  $G$  that maps  $\mathbf{G}_P \mathbf{J}_\pm$  to the circular point-pair at infinity w.r.t. some affine representation of  $\Pi$  in which the circular point-pair only depends on the two scalars  $a$  and  $b$  ; the matrix

$$\mathbf{G}_E = \begin{bmatrix} s\mathbf{R}_2 & \mathbf{t}_2 \\ \mathbf{0}_2^\top & 1 \end{bmatrix} \quad (9)$$

is the Euclidean component of  $G$  i.e., the matrix of a 2D similitude of scaling  $s$ , rotation  $\mathbf{R}_2$  and translation  $\mathbf{t}_2$ .

In our case,  $\mathbf{G}_P$  transforms the images of two concentric circles to two concentric ellipses ;  $\mathbf{G}_A$  transforms these two ellipses to two concentric circles ;  $\mathbf{G}_E$  translates one circle at the origin and scales its radius to 1.

First, in (7), we point out that, as the vector of the vanishing line  $\mathbf{v}$  of  $\Pi$  is the polar line of the image  $\mathbf{u}_Q$  of the centre of the circle w.r.t. the ellipse  $Q$ , it can be replaced by

$$\mathbf{v} \sim \mathbf{q}(\mathbf{u}_Q^\top, 1)^\top = (Q_{11}x_C, Q_{22}y_C, Q_{33})^\top$$

Second, in (8), we can show that  $a$  and  $b$  depend on  $Q$  and  $\mathbf{u}_Q$  the following way. On the hand, since the circular point-pair is invariant under 2D similitude on its plane, we can write that

$$\begin{aligned} \Sigma^* &\sim \mathbf{G}^{-1} \text{diag}(1, 1, 0) \mathbf{G}^{-\top} \\ &\sim \mathbf{G}_P^{-1} \mathbf{G}_A^{-1} \text{diag}(1, 1, 0) \mathbf{G}_A^{-\top} \mathbf{G}_P^{-\top} \end{aligned}$$

On the other hand, the conic dual to the two points at which a conic  $C$  meets a line  $l$  can be written in the form of  $[\mathbf{l}]_\wedge C [\mathbf{l}]_\wedge$  [4, p. 64], where  $[\mathbf{l}]_\wedge$  denotes the skew-symmetric matrix of  $l$  such that  $[\mathbf{l}]_\wedge \mathbf{m} = l \wedge \mathbf{m}$ , for any  $\mathbf{m} \in \mathbb{R}^3$ . This yields, in particular for the conic dual to images of the circular point-pair

$$\Sigma^* \sim [\mathbf{Qc}]_\wedge Q [\mathbf{Qc}]_\wedge \quad (10)$$

since, by definition, the circular point-pair is where the line at infinity of  $\Pi$  meets any circle, which is a property preserved under perspective projection. Then, we have

$$\begin{aligned} \mathbf{G}_P([\mathbf{Qc}]_\wedge Q [\mathbf{Qc}]_\wedge) \mathbf{G}_P^\top &\sim \mathbf{G}_A^{-1} \text{diag}(1, 1, 0) \mathbf{G}_A^{-\top} \\ \Leftrightarrow \underbrace{\begin{bmatrix} ([\mathbf{Qc}]_\wedge Q [\mathbf{Qc}]_\wedge)_{1:2,1:2} & 0 \\ 0 & 0 \end{bmatrix}}_X &\sim \begin{bmatrix} a^2 + b^2 & a & 0 \\ a & 1 & 0 \\ 0 & 0 & 0 \end{bmatrix} \end{aligned}$$

that is a projective equation which can exactly solved for  $a = X_{12}/X_{22}$  et  $b = \sqrt{X_{11}/X_{22} - a^2}$  leading to

$$a = -(Q_{22}u_Q v_Q)/k_1 \quad (11)$$

$$b = \sqrt{-k_2 Q_{22}/(Q_{11} k_1^2)} \quad (12)$$

where  $k_1$  and  $k_2$  are defined in (3) and (4) respectively. From now on, without any loss of generality, we can assume in (3) and (4) that  $k_1$  and  $k_2$  are strictly negative, by choosing the convention that any point  $\mathbf{u}$  inside the ellipse  $Q$  is such that  $(\mathbf{u}^\top, 1)\mathbf{q}(\mathbf{u}^\top, 1)^\top < 0$ . At this step, can easily compute the formal expression using a symbolic software like MAPLE

$$\mathbf{G}_A \mathbf{G}_P \sim \text{diag}\left(-\frac{1}{\sqrt{-k_2 Q_{22}/Q_{11}}}, 1, 1\right) \begin{bmatrix} Q_{11}u_Q^2 - 1 & Q_{22}u_Q v_Q & 0 \\ 0 & 1 & 0 \\ Q_{11}u_Q & Q_{11}v_Q & -1 \end{bmatrix}$$

so

$$(\mathbf{G}_A \mathbf{G}_P)^{-1} \sim \begin{bmatrix} -1 & -Q_{22}u_Q v_Q & 0 \\ 0 & k_1 & 0 \\ -Q_{11}u_Q & -Q_{22}v_Q & -k_1 \end{bmatrix} \text{diag}(\sqrt{-k_1 Q_{22}/Q_{11}}, -1, -1)$$

Third, since by applying  $G_{\mathcal{A}}G_{\mathcal{P}}$  to  $\mathbb{Q}$  we obtain a circle, in order to translate it to the origin and scale its radius to 1, i.e., to obtain a circle with matrix  $\text{diag}(1, 1, -1)$  we seek  $x, y$  and  $\sigma$  in

$$G_{\mathcal{E}} = \begin{bmatrix} \sigma & 0 & \sigma x \\ 0 & \sigma & \sigma y \\ 0 & 0 & 1 \end{bmatrix} \quad (13)$$

such that

$$(G_{\mathcal{A}}G_{\mathcal{P}})^{-\top} \mathbb{Q} (G_{\mathcal{A}}G_{\mathcal{P}})^{-1} \sim G_{\mathcal{E}} \begin{bmatrix} 1 & 0 & 0 \\ 0 & 1 & 0 \\ 0 & 0 & -1 \end{bmatrix} G_{\mathcal{E}}^{\top}$$

and get as solutions :

$$\begin{cases} x = u_Q / \sqrt{-k_1 Q_{22} / Q_{11}} \\ y = v_Q / k_1 \\ \sigma = \sqrt{-k_2 Q_{22}} \end{cases} \quad (14)$$

After some little algebra, introducing a variable  $\mathbf{u}$  such that  $G(\mathbf{u}_q) = G_{\mathcal{E}}G_{\mathcal{A}}G_{\mathcal{P}}$ , we obtain the matrix  $G(\mathbf{u})$  as expressed in the proposition 2, and thus complete the proof.  $\square$

## References

- [1] F. Bergamasco, A. Albarelli, E. Rodolà, and A. Torsello. Rune-tag: A high accuracy fiducial marker with strong occlusion resilience. In *Proceedings of the 2011 IEEE Conference on Computer Vision and Pattern Recognition (CVPR2011)*, pages 113–120, 2011.
- [2] J. Canny. A computational approach to edge detection. *IEEE Trans. Pattern Anal. Mach. Intell.*, 8(6):679–698, 1986.
- [3] O. Gallo and R. Manduchi. Reading 1d barcodes with mobile phones using deformable templates. *IEEE Trans. Pattern Anal. Mach. Intell.*, 33(9):1834–1843, 2011.
- [4] R. Hartley and A. Zisserman. *Multiple View Geometry in Computer Vision*. Cambridge University Press, second edition, 2004.
- [5] H. Kato and M. Billinghurst. Marker tracking and HMD calibration for a video-based augmented reality conferencing system. In *Proceedings 2nd IEEE and ACM International Workshop on Augmented Reality (IWAR'99)*, pages 85–94. IEEE Comput. Soc, 1999.
- [6] M. G. Prasad, S. Chandran, and M. S. Brown. A motion blur resilient fiducial for quadcopter imaging. In *Proceedings of the 2015 IEEE Winter Conference on Applications of Computer Vision (WACV15)*, WACV '15, pages 254–261, Washington, DC, USA, 2015. IEEE Computer Society.
- [7] M. Toyoura, H. Aruga, M. Turk, and X. Mao. Mono-spectrum marker: an AR marker robust to image blur and defocus. *The Visual Computer*, 30(9):1035–1044, Dec. 2013.
- [8] D. Wagner and D. Schmalstieg. ARToolKitPlus for Pose Tracking on Mobile Devices. In *Proceedings of 12th Computer Vision Winter Workshop CVWW07*, pages 139–146, 2007.